Supplementary Information for

High performance plain carbon steels obtained through 3D-printing

Qiyang Tan[1†], Haiwei Chang[1†], Guofang Liang[1], Vladimir Luzin[2,3], Yu Yin[1], Fanshuo Wang[1], Xing Cheng[4], Ming Yan[4], Qiang Zhu[4], Christopher Hutchinson[5,*], Ming-Xing Zhang[1,*]

[1]School of Mechanical and Mining Engineering, The University of Queensland, QLD 4072, Australia

[2]Australian Nuclear Science and Technology Organization (ANSTO), NSW 2234, Australia

[3]School of Engineering, The University of Newcastle, Callaghan, NSW 2308, Australia

[4]Department of Materials Science and Engineering and Shenzhen Key Laboratory for Additive Manufacturing of High-performance Materials, Southern University of Science and Technology, Shenzhen 518055, China

[5]Department of Materials Science and Engineering, Monash University, VIC 3800, Australia

Corresponding authors: christopher.hutchinson@monash.edu, mingxing.zhang@uq.edu.au,
[†]These authors contributed equally to this work

Supplementary Section 1. Hardness distributions in 3D-printed 1040 steel.

We conducted hardness test on the 3D-printed 1040 steel. Supplementary Fig. 1 shows the indentation impressions and Rockwell hardness distributions across the XZ-plane (i.e. longitudinal plane along the BD) on the 3D-printed 1040 steel. The sample exhibits a comparable indentation impression size and profile, accompanied by a consistent hardness distribution. This underscores the homogeneous microstructure achieved in the steel.

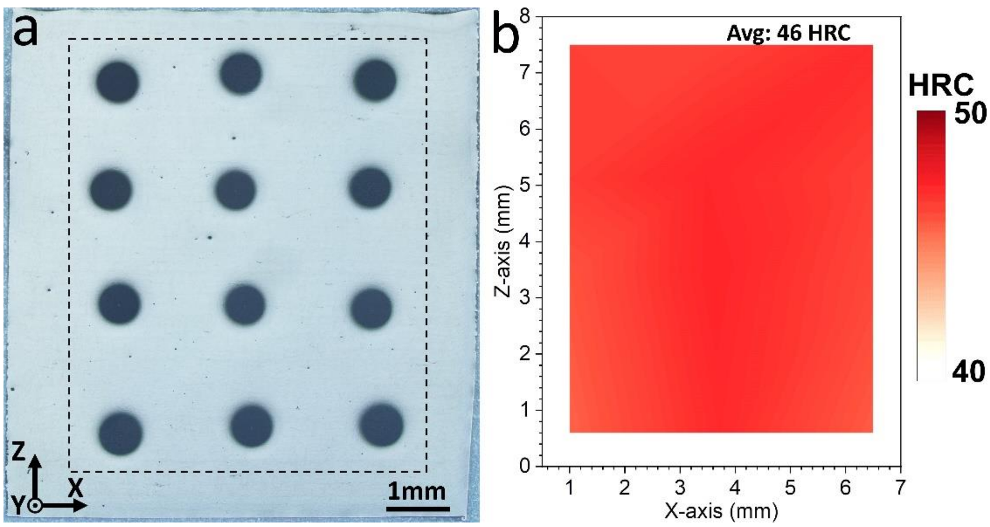

Supplementary Figure 1: *Hardness distribution of 3D-printed 1040 steel. (**a**) Cross-sectional optical micrographs of the 3D-printed 1040 steel after Rockwell hardness testing, demonstrating the similar indentation impressions on each sample. (**b**) Rockwell hardness profile taken from the marked areas in (a) showing uniform hardness distribution. Source data are provided as a Source Data file.*

Supplementary Section 2. Densification behaviour

This preliminary experiment aims to determine the optimal processing parameter set in order to obtain the highly dense 3D-printed plain carbon steels. Supplementary Tables 1 and 2 summarize the 3D-printing parameters and their corresponding laser energy densities calculated by $E = \frac{P}{vht}$ [1].

Supplementary Table 1: PBF processing parameters.

Process parameter and unit	Value
Laser power, P (W)	100, 125, 150, 175, 200, 225, 250, 275, 300, 325, 350, 375
Scanning speed, v (mm/s)	400, 600
Hatching spacing, h (μm)	120
Layer thickness, t (μm)	30
Preheating temperature (°C)	200
Scanning strategy	x/y-raster
Layer rotation angle (°)	33

Supplementary Table 2: The laser energy density corresponding to each processing parameter set. Note that the layer thickness (t) and the hatch space (h) were fixed at 0.03 mm and 0.12 mm, respectively.

Process parameter set	Laser energy density, E
P = 100 W, v = 600 mm/s	46 J/mm^3
P = 125 W, v = 600 mm/s	58 J/mm^3
P = 150 W, v = 600 mm/s	69 J/mm^3
P = 175 W, v = 600 mm/s	81 J/mm^3
P = 200 W, v = 600 mm/s	93 J/mm^3
P = 225 W, v = 600 mm/s	104 J/mm^3
P = 250 W, v = 600 mm/s	116 J/mm^3
P = 275 W, v = 600 mm/s	127 J/mm^3
P = 300 W, v = 600 mm/s	139 J/mm^3
P = 325 W, v = 600 mm/s	150 J/mm^3
P = 350 W, v = 600 mm/s	162 J/mm^3
P = 375 W, v = 600 mm/s	173 J/mm^3
P = 350 W, v = 400 mm/s	243 J/mm^3
P = 375 W, v = 400 mm/s	260 J/mm^3

As seen in Supplementary Fig. 2, Samples with insufficient energy density ($\leq$ 45 J/mm^3) were featured with high fractions of pores, which could be ascribed to the lack of fusion [2]. The sample density increased constantly with increasing the energy density. For both steels, there were wide energy density window, (i.e. 69-174 J/mm^3 for the 1040 steel and 69-150 J/mm^3 for the 1080 steel), of which the pores were virtually eliminated, achieving near-full densification (99.8%). However, further increasing the energy beyond these ranges was associated with excessive energy input, which caused high porosity in both steels presumably due to the keyhole formation [2]. Such broad processing windows for optimal densification demonstrates the remarkable 3D-printability of plain carbon steels.

The hardness of the investigated steels is influenced by the laser energy inputs, with discrepancies arising from changes in cooling rates tied to different energy levels. Notably, reduced energy input is linked to faster cooling rates during melt pool solidification [3]. As a result, variations in processing parameters yield distinct phase compositions and microstructural features, and properties suited to specific applications as demonstrated in Figs. 2-4 in the main text.

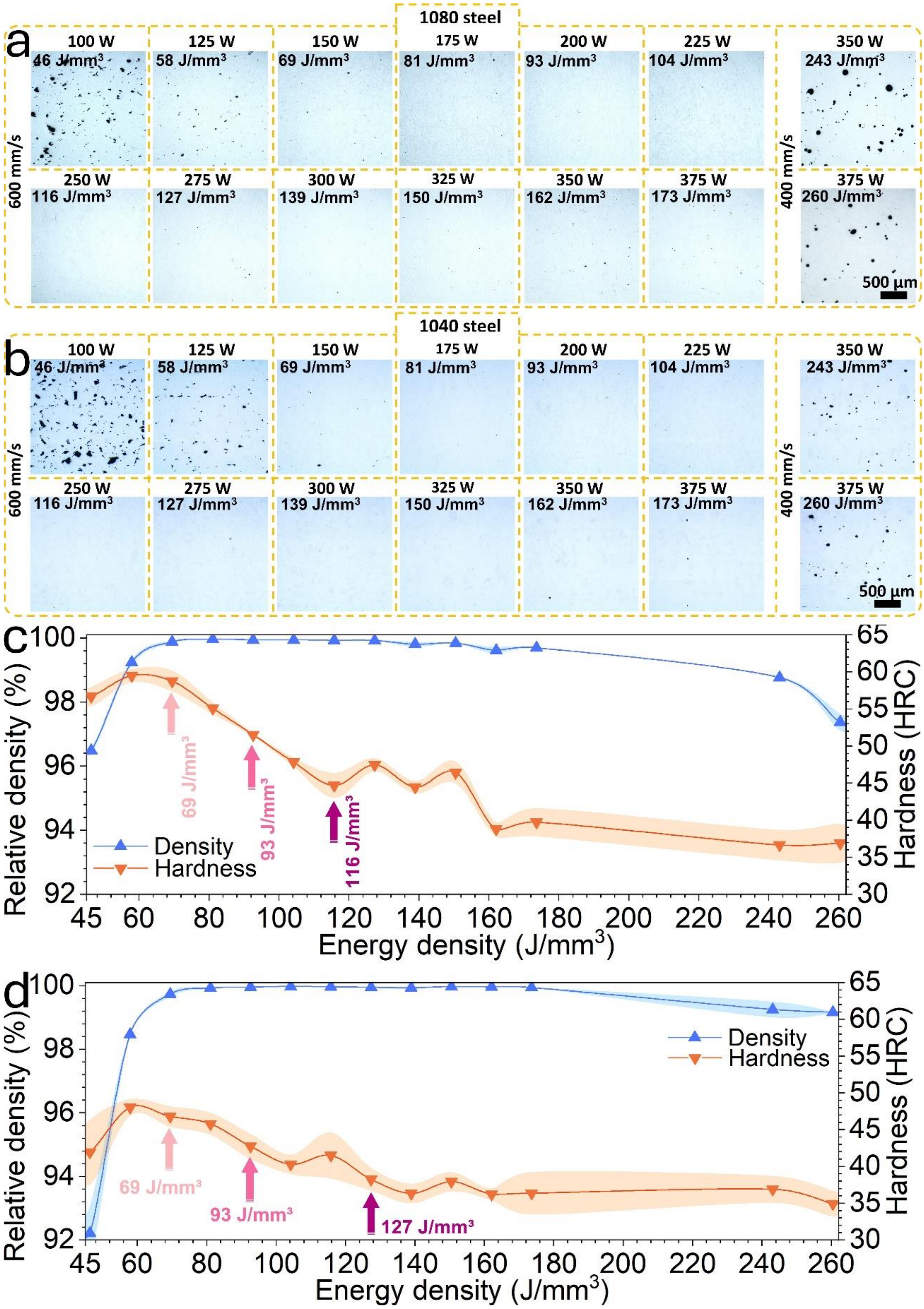

Supplementary Figure 2: *Densification behaviours and hardness of the 3D-printed (**a**, **c**) 1080 steel and (**b**, **d**) 1040 steel at various processing parameters: (**a**, **b**) Longitudinal optical micrographs of samples with different laser powers, (**c**, **d**) the overall sample density and hardness as a function of the volumetric energy density. The arrows in (c) and (d) pinpoint the three chosen samples for each steel subjected to microstructural characterizations and property validation. Source data are provided as a Source Data file.*

Supplementary Section 3. Orientation relationship between α’-blocks and prior γ grain

The orientations of the α’-blocks within a single prior austenite grain was examined using electron backscattered diffraction (EBSD) pole figures as shown in Supplementary Fig. 3. For all 3D-printed 1080 steels, the shapes of “three-fold-stars” are revealed in the {110} pole figures. The sides of these “three-fold-stars” are clearly warped, possessing 18 intensity maxima. This suggests the approximated Greninger-Troiano orientation relationship (i.e. $\{110\}_{\alpha'}||\{111\}_{\gamma}$, $< 5\ 12\ 17 >_{\alpha'} || < 7\ 17\ 17 >_{\gamma}$) between the α’-blocks and the prior γ grains in these steels [4].

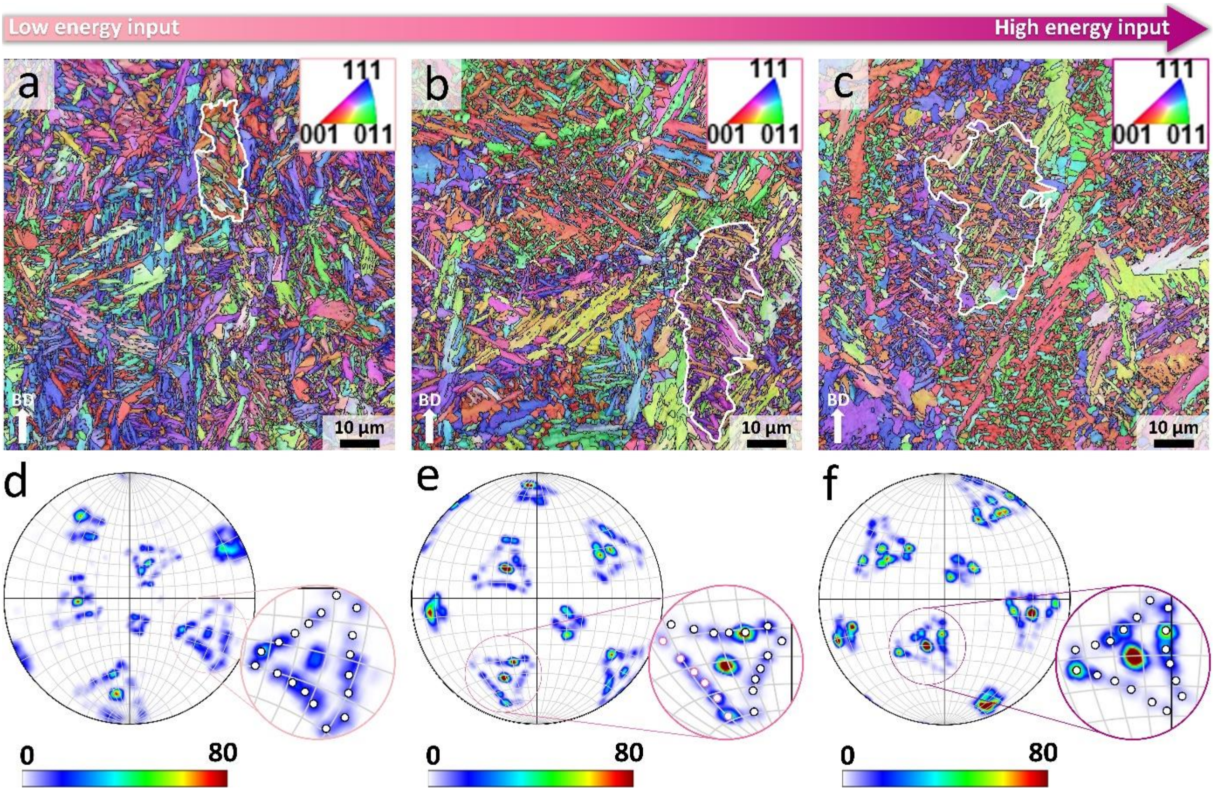

Supplementary Figure 3: *EBSD pole figures analysis. (**a-c**) EBSD-IPF maps of the 3D-printed AISI 1080 steels with various laser energy inputs of (**a**) 69 J/cm³, (**b**) 93 J/cm³ and (**c**) 116 J/cm³, and (**d-e**) the contoured {110} pole figures, showing the α’-block orientations within prior austenite grains marked by the white line in (a-c). The relative intensity of the diffraction peaks are indicated by the colour scale and the 18 intensity maxima on the sides of typical “three-fold-stars” are marked by the solid dots.*

Supplementary Section 4. High-resolution TEM characterization on the low-energy-produced 1080 steel

Supplementary Fig. 4a shows the high-resolution TEM image taken across the α’-Fe/carbide interface in the bainite region. The atomic configurations provide direct evidence confirming the carbide to be θ-Fe_3C. The corresponding fast Fourier transforming (FFT) confirms a well-established orientation relationship between these two phases [5]:

$$[011]_{\alpha'}||[101]_{\theta}, (\bar{2}1\bar{1})_{\alpha'}||(30\bar{3})_{\theta}$$

Supplementary Fig. 4b shows the high-resolution TEM image across the boundary between the α’-matrix and α’-twin in the martensite region. The atomic arrangement reveals the presence of the ω-Fe phase along the twin boundary, spanning several atomic layers with fully coherency with the adjacent α’-Fe phase. The atomic arrangement of this twining structure agrees well with previously simulated results [5-7].

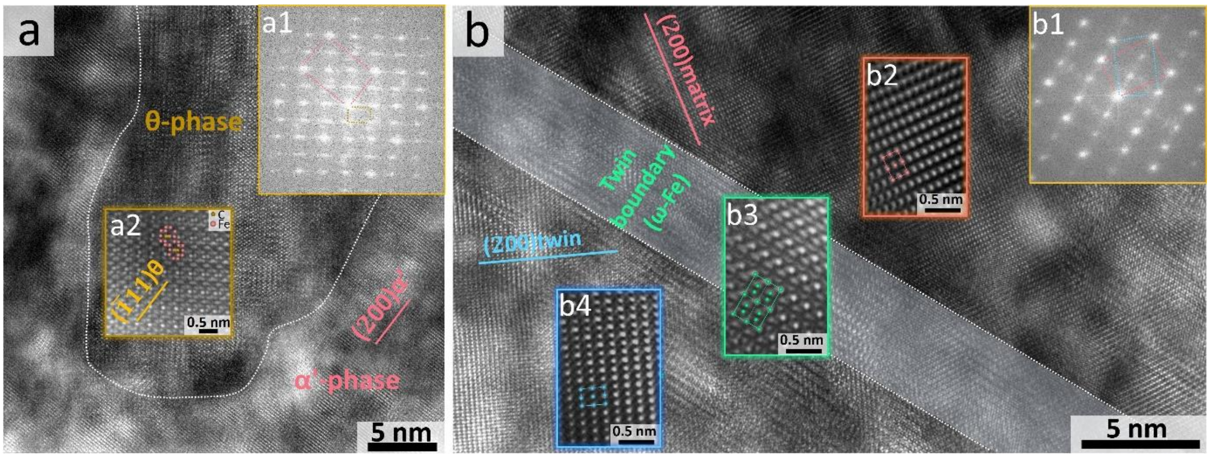

Supplementary Figure 4: *High-resolution TEM images of (**a**) the α'-Fe/carbide interface in a bainite region and (**b**) the twin boundary in a martensite region taken along the $[011]_{\alpha'}$ zone axis, with the insets showing (a1 and b1) the corresponding FFT patterns and (a2, b2-b4) the atomic configurations of the (a2) θ-Fe_3C, (b2) α'-matrix, (b3) ω-Fe and (b4) α'-twin.*

Supplementary Section 5. TEM characterization on the high-energy-produced 1080 steel

TEM characterization was conducted on the 1080 steel produced with high laser energy input of 116 J/mm³. As evident from Supplementary Fig. 5, all the α'-blocks are interspersed with copious θ-Fe_3C, manifesting as either needles or particulates (Supplementary Figs. 5b and e). Indexing the corresponding diffraction patterns (Supplementary Figs. 5c and f) further confirms the following orientation relationships between the α'-and the θ-Fe_3C, which have been frequently reported in carbon steels [8-10]:

$$[111]_{\alpha'}||[311]_{\theta}, (10\bar{1})_{\alpha'}||(\bar{1}03)_{\theta}$$

$$[001]_{\alpha'}||[01\bar{1}]_{\theta}, (\bar{1}\bar{1}0)_{\alpha'}||(022)_{\theta}$$

These are different formats of the Isaichev and the Bagaryatskii orientation relationships, respectively [11,12]. This finding corroborates the bainite-dominant microstructure observed in the sample, aligning with its elevated BC value (Fig. 2g in the main text).

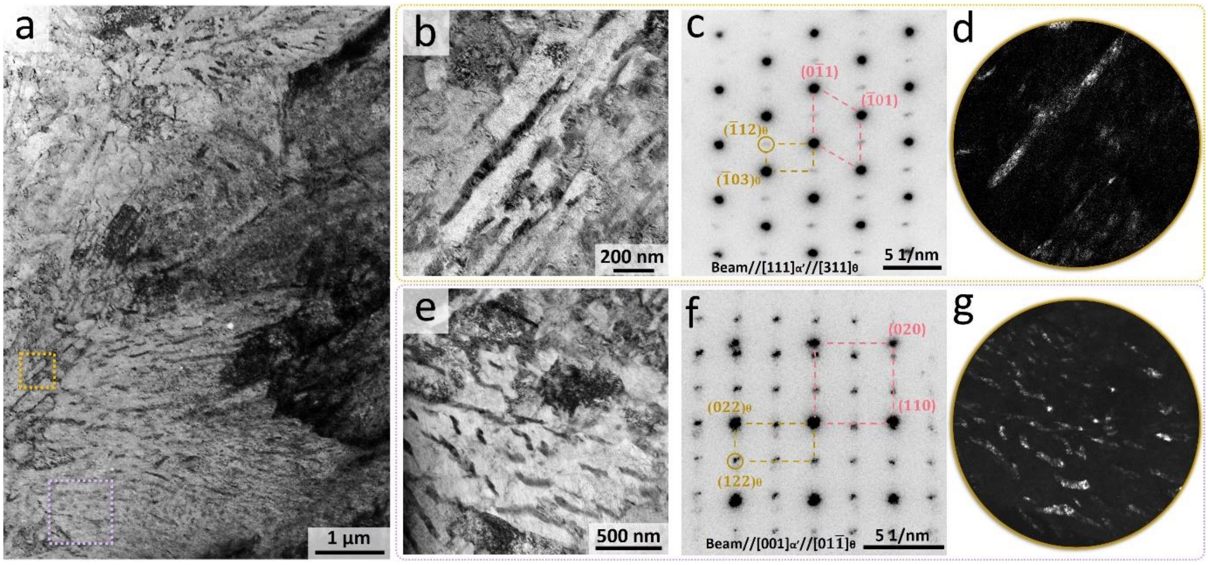

Supplementary Figure 5: *TEM characterization of the 1080 steel produced with high laser energy input of 116 J/mm³. (**a**) Bright-field TEM micrograph showing the bainite-dominant microstructure in this sample. (**b**, **e**) The higher magnified TEM image of the areas marked in (a), taken close to the*

*$[111]_{\alpha'}$ and $[001]_{\alpha'}$ zone axes, respectively. They shows (b) the needle shaped carbide and (e) the carbide nanoparticles in bainite blocks, respectively. (**c**, **f**) the associated diffraction pattern of (b) and (e), respectively, with the electron beam aligned along the $[111]_{\alpha'}$ and $[001]_{\alpha'}$ zone axes, respectively. (**d**, **g**) Dark-field TEM images taken from the diffraction spots marked in (c) and (f), respectively.*

Supplementary Section 6. TEM characterization on the high-energy-produced 1040 steel

TEM characterization was conducted on the 1040 steel produced with high laser energy input of 127 J/mm³. As shown in Supplementary Fig. 6, unlike the nanostructured bainite formed in the low-energy-produced sample, bainite formed in the high-energy-produced sample contains coarser θ-Fe_3C manifesting as either needles or particulates, even though the α'-laths are still at nanometre scale (Supplementary Figs. 6b and e). Indexing the corresponding diffraction patterns (Supplementary Figs. 6c and f) further confirms the following orientation relationships between the α' and the θ-Fe_3C, which have been frequently reported in carbon steels [10,11,13]:

$$[011]_{\alpha'}||[101]_{\theta}, (\bar{2}1\bar{1})_{\alpha'}||(30\bar{3})_{\theta}$$

$$[001]_{\alpha'}||[01\bar{1}]_{\theta}, (\bar{1}\bar{1}0)_{\alpha'}||(022)_{\theta}$$

These are different formats of the Isaichev and the Bagaryatskii orientation relationships, respectively [11,12]. This finding evidences the bainite-dominant microstructure, aligning with its elevated BC value as shown by Fig. 3g in the main text.

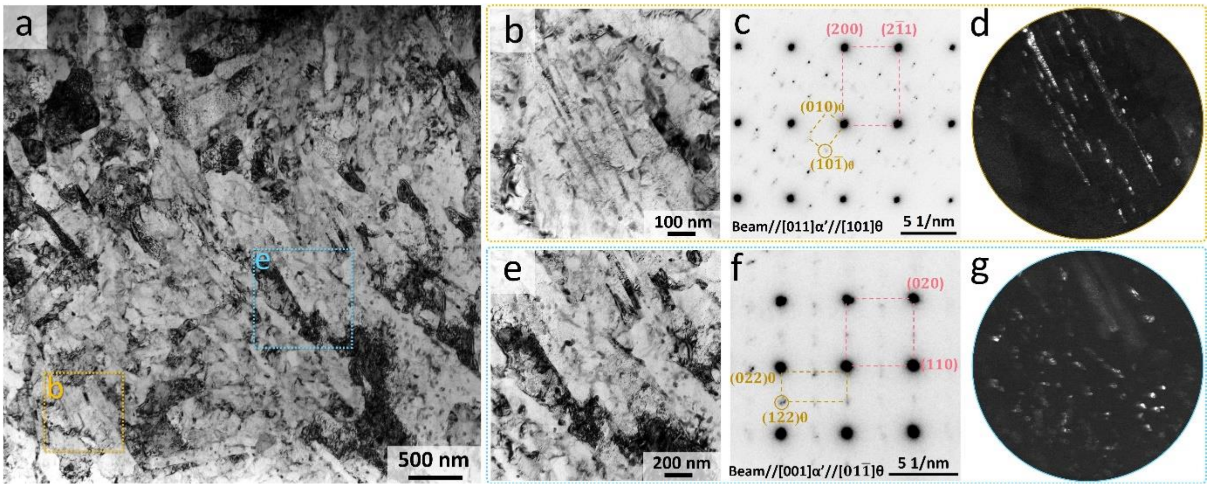

***Supplementary Figure 6:** TEM characterization of the 1040 steel produced with high laser energy input of 127 J/mm³. (**a**) Bright-field TEM micrograph showing the bainite-dominant microstructure in this sample. (**b**, **e**) The higher magnified TEM image of the areas marked in (a), taken close to the $[011]_{\alpha'}$ and $[001]_{\alpha'}$ zone axes, respectively. They shows (b) the needle shaped carbide and (e) the carbide nanoparticles in bainite blocks. (**c**, **f**) the associated diffraction pattern of (b) and (e), with the electron beam aligned along the $[011]_{\alpha'}$ and $[001]_{\alpha'}$ zone axes, respectively. (**d**, **g**) Dark-field TEM images taken from the diffraction spots marked in (c) and (f), respectively.*

Our microstructural observations indicate that the cooling trajectory during 3D-printing effectively bypasses the pearlite formation region of the 1040 steel, ensuring steel hardening at a broad processing window. However, achieving a martensite-dominant microstructure in 1040 steel proves more challenging than in 1080 steel, despite the use of low energy inputs. This could be ascribed to the lower carbon content of 1040 steel, which advances the start of bainitic transformation curve, causing an inevitable intersection with the cooling trajectory at low temperatures. Nevertheless, the fast cooling rate associated with the low energy input allows the formation of nano-sized bainitic laths, akin to those in the recent advocated nano-bainitic steel that commonly requires precise composition design [14-17].

Furthermore, such bainitic microstructure distinguishes itself by hosting nano-scale, metastable ω'-carbides rather than the high fraction of coarser needle or particulate carbides typical of conventional bainite [18]. This suggests the suppression of cementite precipitation by rapid cooling and substantial remaining carbon supersaturation within the bainitic α'-laths. Thus, a good strength-ductility-toughness synergy is achieved in this steel as evidenced by our mechanical testing (Fig. 4 in the main text).

Supplementary Section 7. Effect of tempering on the microstructure of 3D-printed 1080 steel

TEM characterization was conducted on the low-energy-produced 1080 steel (69 J/mm³) after tempering at 300 °C and 350 °C for 2 hours. In contrast to the nano-twined substructure in the as-printed sample, tempering at 300 °C initiates the detwinning and carbon desaturation. As exemplified in Supplementary Fig. 7a, the α'-lath in the sample tempered at 300 °C only consists of a few $\{112\} < 111 >$ – type twins, corroborated by the diffraction pattern (Supplementary Fig. 7b) and dark-field TEM image (Supplementary Fig. 7c). Localized electron diffraction analysis within the α'-matrix unveils additional weak diffraction spots that belong to ω'-carbide. These carbides exhibit several to tens of nanometres in size, distributing mainly along the twin boundaries, as confirmed by the corresponding dark-field TEM image shown in Supplementary Fig. 7e. Moreover, the atomic configuration of the ω'-carbide (Supplementary Fig. 7h) is highly consistent with the structure of ω'-Fe_3C along its [001] axis proposed by Ping et al. [5,19,20]. Indexing the corresponding FFT pattern (Supplementary Fig. 7f) according to the ω'-Fe_3C model suggests the OR between α' and ω' as follows:

$$[011]_{\alpha'}||[100]_{\omega'}, (0\bar{1}1)_{\alpha'}||(012)_{\omega'}$$

Recent studies have demonstrated that ω'-phase is a precursor to the stable θ-Fe_3C cementite, evolving from the interfacial-twin-boundary ω-phase upon tempering [5,19]. The identification of this metastable phase, along with the partially detwinned features displayed in Supplementary Fig. 7 underscore the partially tempered nature of the 1080 steel at this temperature.

Increasing the temperature to 350 °C led to a fully tempered microstructure where all α' laths are devoid of twinning but replete with a dense distribution of nano-sized carbides manifesting predominantly as needles or discrete particles (Supplementary Figs. 8a, b and d). Supplementary Figs. 8c-g shows the selected area diffraction pattern captured from a single α'-lath alongside a high-resolution TEM image taken across the α'-Fe/carbide interface. Indexing the diffraction pattern and the atomic arrangements furnishes direct evidence confirming the carbide as the stable θ-Fe_3C phase. The corresponding dark-field TEM image also evidences that most of the θ-phase particles possess a preferential alignment relative to the α'-lath, indicating their nucleation along the pre-existing twin boundaries. This observation aligns with the recognized pathway for cementite precipitation (i.e. ω → ω' → θ' → θ) that initiates from the interfacial-twin-boundary ω-phase [20]. Moreover, we also observed the following orientation relationship between the α' and the θ-Fe_3C, which is a different format of the Bagaryatskii orientation relationship [12] and has previously reported in tempered martensitic steels [21]:

$$[111]_{\alpha'}||[010]_{\theta}, (2\bar{1}\bar{1})_{\alpha'}||(002)_{\theta}$$

The microstructure we observed here indicates the occurrence of detwinning and carbon desaturation in the 3D-printed 1080 steel upon tempering. Such a microstructural evolution is attributed to the thermally induced carbon redistribution, dislocation rearrangement and annihilation, and migration of twin boundaries facilitated by the transition from metastable ω-Fe into stable θ-Fe_3C/α-Fe [5,19,20,22,23]. The transformation of nano-twined, high-carbon martensite to lath martensite interspersed with nano-cementite is anticipated to provide a higher resistance against crack initiation and propagation, offering increased toughness and ductility. This hypothesis is substantiated by our mechanical testing as discussed in the next session.

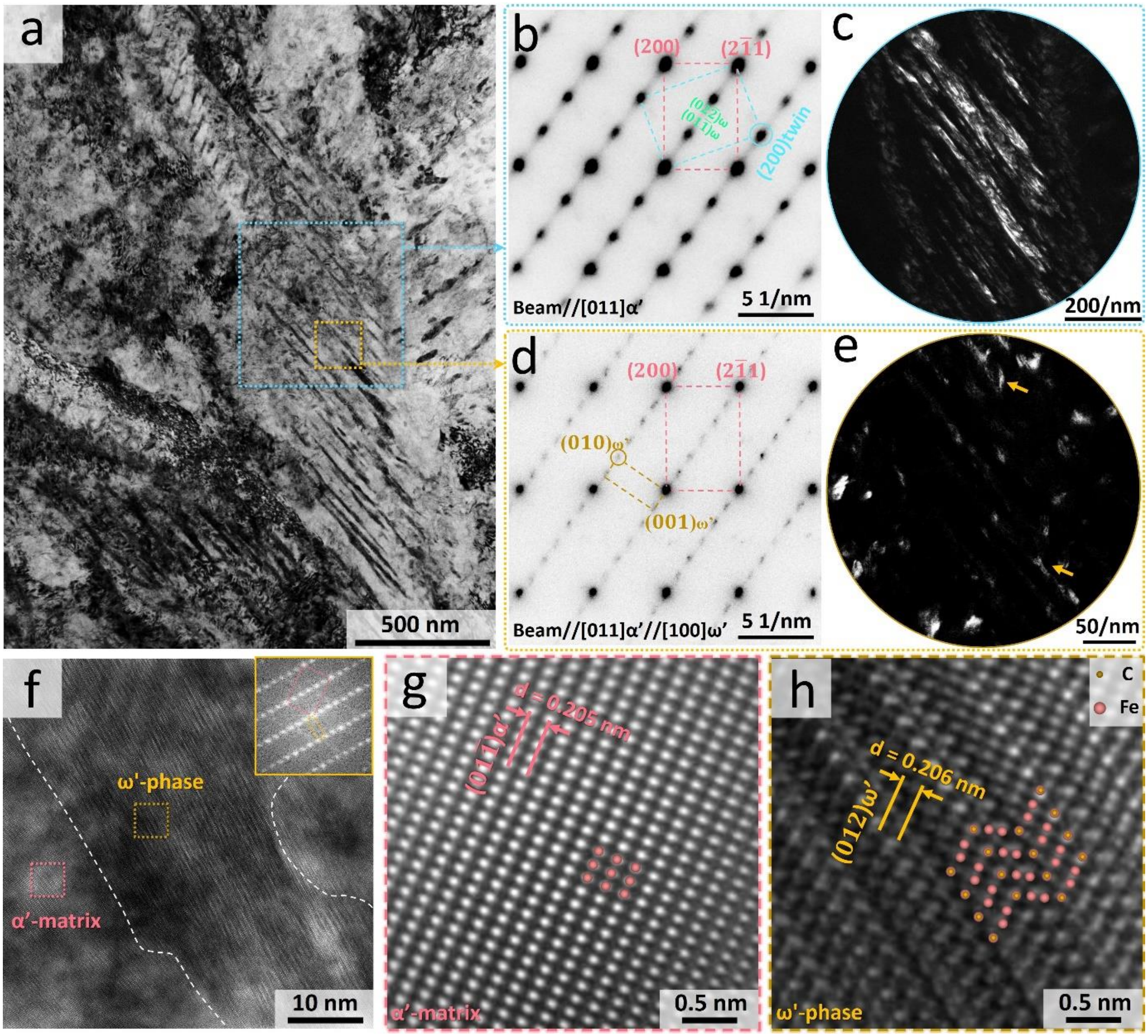

Supplementary Figure 7: *TEM characterization of the low-energy-produced 1080 steel (69 J/mm³) after tempering at 300 °C for 2 hours. (**a**) Bright-field TEM micrograph showing partial detwinning in lath martensite microstructure. (**b**) Diffraction pattern of the areas marked in (a), with the electron beam aligned along the* $[011]_{\alpha'}$ *axis, showing the typical* $\{112\} < 111 >$ *– type twining in the α'-lath. (**c**) Localized diffraction pattern taken at the untwined α'-matrix, showing the existence of extra spots that belongs to the ω'-Fe₃C phase. (**c, e**) Dark-field TEM images taken from the diffraction spot marked in (b) and (d), respectively. The arrows marked in (e) shows indicates the ω'-Fe₃C nanoparticles along the twin boundaries. (**f**) High-resolution TEM images of the α'-Fe/ω'-Fe₃C interface taken along the* $[011]_{\alpha'}$ *zone axis, with the inset showing the corresponding FFT pattern. (**g**, **h**) Magnified views of marked areas in (e), showing the atomic configurations of (g) α'-matrix and (h) ω'-Fe₃C.*

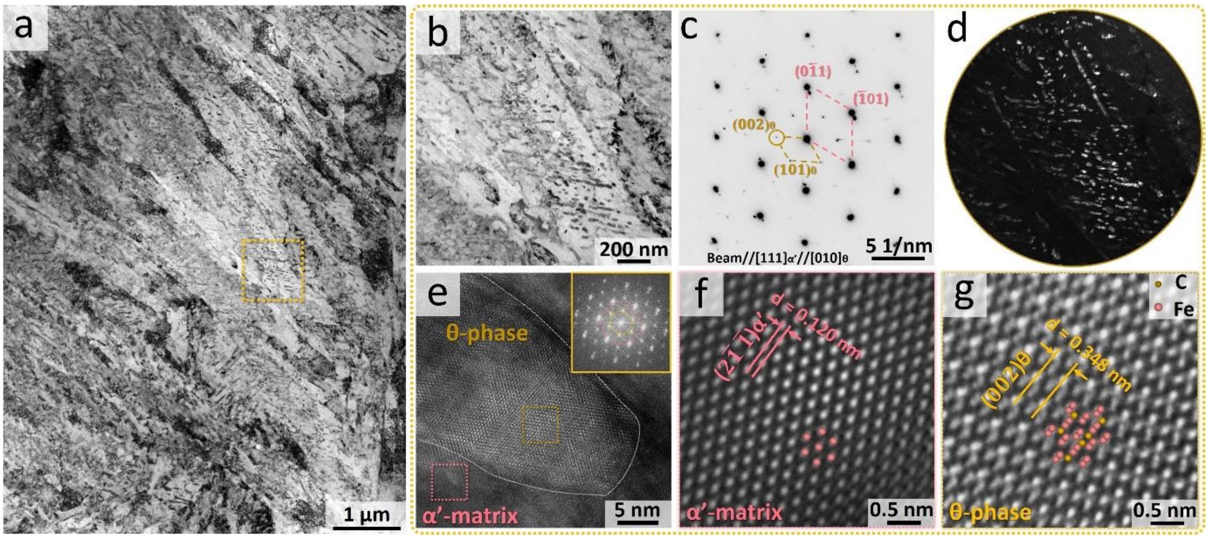

Supplementary Figure 8: *TEM characterization of the low-energy-produced 1080 steel (69 J/mm³) after tempering at 350 °C for 2 hours. (**a**) Bright-field TEM micrograph showing the lath martensite microstructure in this sample. (**b**) The higher magnified TEM image of the areas marked in (a), taken close to the* $[111]_{\alpha'}$ *zone axis, showing the nano-sized carbides in a single α'-lath. (**c**) The associated diffraction pattern of (b), with the electron beam aligned along the* $[111]_{\alpha'}$ *axis. (**d**) Dark-field TEM images taken from the diffraction spot marked in (c), showing needle or particulate morphologies of the carbides. (**e**) High-resolution TEM images of the α'-Fe/carbide interface taken along the* $[111]_{\alpha'}$ *zone axis, with the inset showing the corresponding FFT pattern. (**f**, **g**) Magnified views of marked areas in (e), showing the atomic configurations of the (f) α'-matrix and (g) θ-Fe_3C.*

Supplementary Section 8. Effect of tempering on the mechanical properties of 3D-printed plain carbon steels

To further elucidate the impact of tempering on the tensile properties and Charpy impact toughness of 3D-printed plain carbon steels, the as-printed samples were subjected to a direct tempering at 300 °C, 350 °C and 400 °C for 2 hours. Supplementary Fig. 9 displays engineering stress-strain curves of the 3D-printed 1080 and 1040 steels at different tempering conditions. The determined yield strength (YS), ultimate tensile strength (UTS), elongation to fracture (El) and impact toughness are summarized in Supplementary Table 3. It is evident that the mechanical properties of 1080 steel are markedly affected by tempering when produced with a low-energy input (i.e. martensite prevails). The low-energy-produced 1080 steel achieves a high UTS of 1976 MPa, but paralleled by its limited uniform plastic deformation with an overall El of only 3.5% and low impact energy of 6 J. Such brittleness also creates challenge in precise determination of the yield strength (YS) from the stress-strain curves. This observation indicates that despite the in-situ tempering effect from the cyclical thermal nature of the layer-wise 3D-printing, the embrittlement nature of high-carbon martensite (as proved by Fig. 2 in the main text) cannot be completely mitigated. Such embrittlement arises from its highly supersaturated solid solution, significant internal stresses and a high density of dislocations and twins [18].

A low-temperature tempering at 300 °C reduces this embrittlement, improving the El to 5.5% and the impact toughness to 8 J. The stress-strain curve shown in Supplementary Fig. 9b also confirms the presence of necking, indicating a transition towards ductile fracture. It is noteworthy that the low-temperature tempering substantially enhances the ductility without sacrifice the strength of the 1080 steel, evidenced by its high YS of 1733 MPa and UTS of 1983 MPa. This seems to be controversial to traditional wisdom that tempering commonly softens martensite [18]. This paradox can be understood by the concurrent processes of tempering-induced recovery and strengthening. During tempering, martensite softening occurs through processes such as detwinning, dislocation annihilation, and carbide desaturation, whilst strengthening is induced by dislocation rearrangement into low-angle cell boundaries and precipitation of finely distributed carbides that pin dislocations and impede plastic deformation [18,24,25]. For the present 1080 steel, tempering at 300 °C led to a partially tempered microstructure (Supplementary Fig. 7), which is likely to create a dominance of strengthening over recovery, thus attenuating the brittleness of martensite while maintaining the strength.

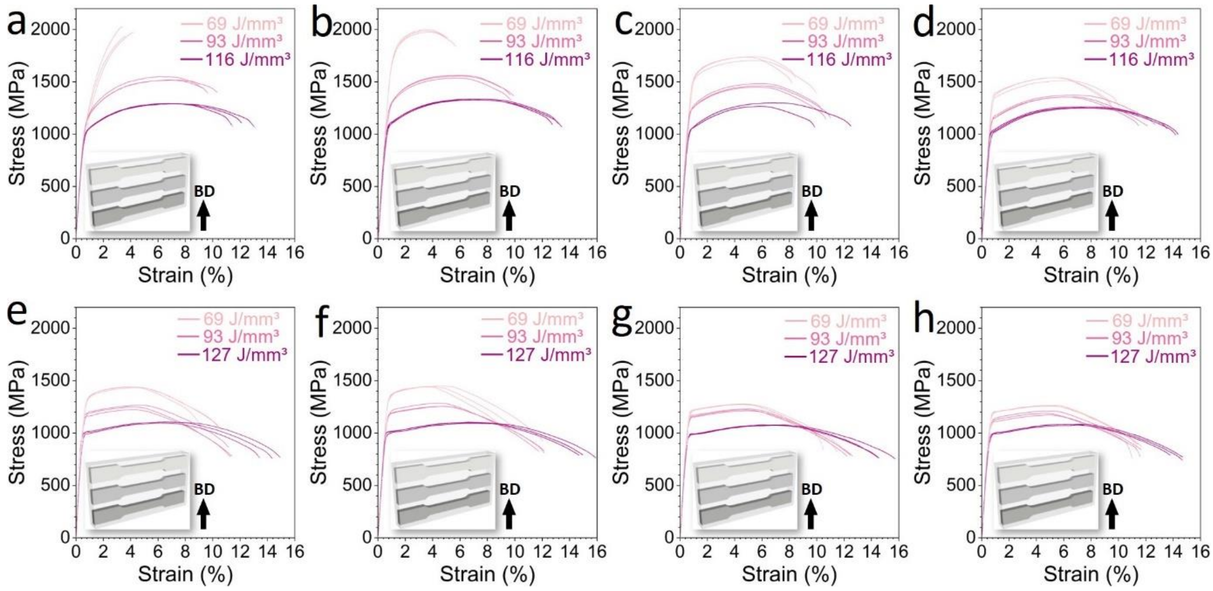

Supplementary Figure 9: *Typical engineering tensile stress-strain curves of the 3D-printed (a-d) 1080 steels and (e-h) 1040 steels at (a, e) as-printed condition, and after tempering for 2 hours at (b, f) 300 °C, (c, g) 350 °C and (d, h) 400 °C, with insets and arrows showing the sample sectioning orientation and building direction (BD), respectively. Source data are provided as a Source Data file.*

Increasing the tempering temperature to 350 °C led to complete detwinning and formation of a high fraction of nano-sized carbides within α’-laths, signifying a fully tempered microstructure (Supplementary Fig. 8). The fully tempered α' laths interspersed with nano-sized carbides offer enhanced cracking resistance and preserve strength. Thus, a more harmonized strength-ductility-toughness synergy was achieved in this sample, showing a YS of 1533 MPa, UTS of 1726 MPa, El of ~10% and impact toughness of 11 J. Further increasing the tempering temperature to 400 °C led to a further decrease in strength and improvements in ductility and impact toughness, signifying an enhanced the recovery process at higher temperature.

In contrast, tempering treatments exert a limited impact on 3D-printed 1080 steels produced with medium or high energy inputs where bainite prevails (as proved by Fig. 2 in the main text). As shown in Supplementary Fig. 9b, tempering at 300 °C induces marginal changes to the mechanical behaviour of the medium-energy-produced sample. Increasing the tempering temperature to 400 °C slightly softens the steel, characterized by a strength reduction of approximately 150 MPa, whereas it increases ductility to 12%, and impact toughness to 20 J. The high-energy-produced sample, characterized by a bainite-dominant microstructure, showed an even more pronounced resistance to tempering. As depicted in Supplementary Figs. 9b-d and Supplementary Table 3, tempering between 300 °C to 400 °C results in negligible alterations in the strength, ductility and impact toughness of these samples.

Unlike the 1080 steel, the 1040 steel exhibits harmonized strength-ductility-toughness synergy directly after 3D-printing (Supplementary Fig. 9e). Tempering has a limited impact on the mechanical properties of 3D-printed 1040 steels, where bainite prevails at all selected energy inputs (as proved by Fig. 3 in the main text). As shown in Supplementary Figs. 9f-h and Supplementary Table 3, tempering at higher temperatures (350-400 °C) slightly reduces the strength of the sample produced with low energy input, yet its ductility and impact toughness are preserved. Such a slight softening may be attributed to tempering of the small fraction of martensite present in this sample (as proved by Fig. 3 in the main text). However, for all other samples, tempering within the range of 300-400 °C marginally affects the mechanical properties, regardless of the energy input used.

Supplementary Table 3: *Mechanical properties of 3D-printed plain carbon steels at different heat-treated conditions*

Dominant phase	Condition	YS (MPa)	UTS (MPa)	El (%)	Impact toughness
3D-printed 1080					
Martensitic dominance (low E)	As-printed	-	1976 ± 48	3.5 ± 0.4	6 ± 1
	T300 °C	1733 ± 15	1983 ± 15	5.5 ± 0.4	8 ± 1
	T350 °C	1533 ± 15	1726 ± 22	9.2 ± 0.9	11 ± 1
	T400 °C	1363 ± 25	1530 ± 17	9.7 ± 0.4	12 ± 1
Martensite & bainite (medium E)	As-printed	1140 ± 17	1527 ± 20	9.7 ± 0.6	13 ± 1
	T300 °C	1247 ± 38	1553 ± 15	9.8 ± 0.2	15 ± 1
	T350 °C	1223 ± 15	1463 ± 15	10.7 ± 0.3	18 ± 0
	T400 °C	1150 ± 10	1358 ± 10	12.1 ± 0.6	20 ± 1
Bainitic dominance (high E)	As-printed	1025 ± 3	1292 ± 1.5	12.3 ± 0.8	22 ± 0
	T300 °C	1093 ± 12	1328 ± 5	13.1 ± 0.3	21 ± 2
	T350 °C	1041 ± 2	1279 ± 23	11.2 ± 1.8	21 ± 2
	T400 °C	1040 ± 10	1254 ± 6	14.1 ± 0.5	23 ± 2
3D-printed 1040					
Martensite & bainite (low E)	As-printed	1335 ± 5	1430 ± 5	10.2 ± 0.9	30 ± 1
	T300 °C	1350 ± 10	1445 ± 5	10.3 ± 1.5	31 ± 2
	T350 °C	1193 ± 6	1271 ± 4	11.2 ± 0.7	34 ± 2
	T400 °C	1175 ± 11	1253 ± 6	11.5 ± 0.2	37 ± 2
Bainitic dominance (medium E)	As-printed	1177 ± 15	1247 ± 25	11.3 ± 0.1	76 ± 2
	T300 °C	1182 ± 16	1264 ± 21	12.0 ± 0.2	80 ± 1
	T350 °C	1133 ± 15	1219 ± 9	12.4 ± 0.2	80 ± 2
	T400 °C	1092 ± 19	1189 ± 17	11.5 ± 0.3	78 ± 7
Complete bainite (high E)	As-printed	1000 ± 7	1100 ± 7	14.3 ± 0.8	106 ± 5
	T300 °C	1003 ± 11	1103 ± 7	15.3 ± 0.7	111 ± 1
	T350 °C	975 ± 5	1071 ± 4	15.0 ± 0.7	112 ± 1
	T400 °C	965 ± 5	1072 ± 8	14.5 ± 0.6	109 ± 2

This result underscores substantial tempering resistance of bainite compared to martensite in 3D-printed plain carbon steels. The remarkable strength of the martensitic 1080 steel arises from nano-twin boundaries and carbon supersaturated solid solution within the martensitic ferrite (as proved by Fig. 2 in the main text) [18,26]. Accordingly, its strength declines sharply with the progression of detwinning and carbon desaturation during tempering. In contrast, the tempering resistance of bainite can be attributed to the bainitic feature in plain carbon steels and the 3D-printing process. Bainitic transformation inherently involves auto-tempering, where majority of carbon solute precipitates as carbides or partitions from bainitic ferrite [27]. On the other hand, tempering response of bainitic steels is primarily influenced by the decomposition of retained austenite into ferrite and carbide [28]. However, as confirmed by our TEM observation (Fig. 3 in main text and Supplementary Fig. 5), the plainified composition leads to the absence of retained austenite after bainite transformation in both 3D-printed 1080 and 1040 steels, diverging from most alloy steels where retained austenite commonly exists. Furthermore, the cyclical thermal nature of the layer-wise 3D-printing induces in-situ tempering, rendering the as-printed bainite in a condition akin to low-temperature tempering, as opposed to the “fresh” bainite obtained via conventional quenching. Thus, it is not surprising that the post tempering response is rather insensitive in the sample. This feature accentuates the convenience and efficacy of 3D-printing for fabricating bainitic plain carbon steels, particularly the 1040 steel, obviating the need for subsequent heat treatment.

Supplementary Section 9. Evaluation of the anisotropy in mechanical properties

To further assess property anisotropy in the 3D-printed plain carbon steels, additional tensile tests were conducted along the vertical direction (i.e., the build direction) on the 1040 steel. Supplementary Fig. 10 compares the engineering stress-strain curves of the as-printed 1040 steels in both vertical and horizontal directions. The determined YS, UTS, El, and the corresponding calculated anisotropy ratios are summarized in Supplementary Table 4. Except for a moderate anisotropy observed in the low-energy-produced samples, the samples produced with medium and high energy inputs exhibited marginal anisotropy in the tensile properties. This result demonstrates that microstructural refinement through martensitic and/or bainitic phase transformations reduced the anisotropy, effectively addressing the common issue of columnar structures in 3D-printed alloys.

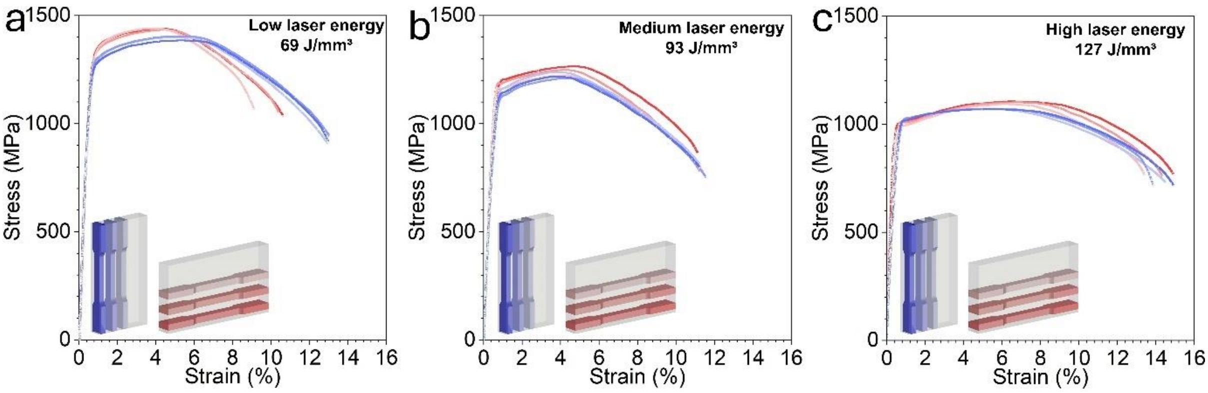

Supplementary Figure 10: *Representative engineering tensile stress-strain curve of the 3D-printed 1040 steel with (a) low laser energy of 69 J/mm^3, (b) medium laser energy of 93 J/mm^3 and high laser energy of 127 J/mm^3 along both horizontal and vertical directions. Source data are provided as a Source Data file.*

Supplementary Table 4: *Mechanical properties of 3D-printed 1040 steels in different directions, with calculated anisotropy ratios. Note that anisotropy ratios were not calculated when property variations fell within the error margins.*

Dominant phase	Direction	YS (MPa) Anisotropy ratio (%)	UTS (MPa) Anisotropy ratio (%)	El (%) Anisotropy ratio (%)
Martensite & bainite (low *E*)	Horizontal	1335 ± 5	1430 ± 5	10.2 ± 0.9
	Vertical	1267 ± 15	1397 ± 10	12.9 ± 0.2
	Anisotropy ratio	-5%	-2%	+26%
Bainitic dominance (medium *E*)	Horizontal	1177 ± 15	1247 ± 25	11.3 ± 0.1
	Vertical	1125 ± 23	1223 ± 16	11.5 ± 0.1
	Anisotropy ratio	-4%	-	-
Complete bainite (high *E*)	Horizontal	1000 ± 7	1100 ± 7	14.3 ± 0.8
	Vertical	992 ± 10	1070 ± 2	14.4 ± 0.6
	Anisotropy ratio	-	-3%	-

Supplementary Section 10. Powder feedstock

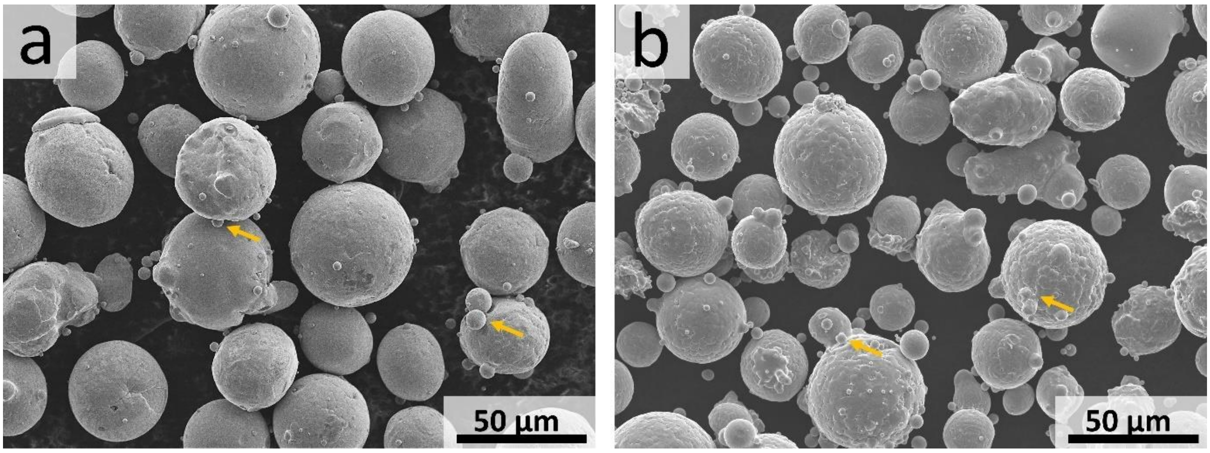

Supplementary Figure 11: *Powder morphology of (a) pure iron and (b) AISI 1080 steel, with arrows indicating small satellites attached to the surface of the spherical powders.*

Supplementary References

1. Simchi, A. Direct laser sintering of metal powders: Mechanism, kinetics and microstructural features. *Materials Science and Engineering: A* **428**, 148-158 (2006).
2. Tan, Q. et al. Effect of processing parameters on the densification of an additively manufactured 2024 Al alloy. *J. Mater. Sci. Technol.* **58**, 34-45 (2020).
3. DebRoy, T. et al. Additive manufacturing of metallic components – Process, structure and properties. *Prog. Mater. Sci.* **92**, 112-224 (2018).
4. Sun, D. et al. Optimization scheme of the orientation relationship from crystallographic statistics of variants and its application to lath martensite. *Mater. Des.* **195**, 109022 (2020).
5. Ping, D. H. et al. A transition of ω-Fe3C → ω′-Fe3C → θ′-Fe3C in Fe-C martensite. *Sci. Rep.* **10**, 6081 (2020).
6. Ikeda, Y. et al. ω structure in steel: A first-principles study. *J. Alloys and Compd.* **684**, 624-627 (2016).
7. Chen, Y. et al. An atomic mechanism for the formation of nanotwins in high carbon martensite. *J. Alloys and Compd.* **767**, 68-72 (2018).
8. Huang, X. et al. Crystallography and morpholgy of cementite precipitates formed during rapid solidification of a ferritic stainless steel. *Acta Mater.* **48**, 4073-4082 (2000).
9. Zhong, N. et al. Orientation Relationships between Ferrite and Cementite by Edge-to-edge Matching Principle. *J. Mater. Sci. Technol.* **27**, 475-480 (2011).
10. Drillet, J. et al. Nanometric Scale Investigation of Phase Transformations in Advanced Steels for Automotive Application. *Metall. Mater. Trans. A* **43**, 4947-4956 (2012).
11. Zhang, M.X. et al. Accurate Orientation Relationships Between Ferrite and Cememtite in Pearlite. *Scr. Mater.* **37**, 2009-2015 (1997).
12. Bagaryatskii, Y. A. *The probable mechanism of the martensite decomposition*. (H. Brutcher Technical Translations, 1950).
13. Liu, T. et al. TEM and electron diffraction analysis of ω-Fe to cementite transformation in quenched and tempered high carbon steels. *AIP Advances* **9,** 045219 (2019).
14. Kumar, A. et al. Mechanical properties of nanostructured bainitic steels. *Materialia* **15**, 101034 (2021).
15. Bhadeshia, H. Nanostructured bainite. *Proceedings of the Royal Society A: Mathematical, Physical and Engineering Sciences* **466**, 3-18 (2010).
16. Kumar, A. et al. Compositional design of high strength nanostructured bainite. *Mater. Res. Express* **6**, 026526 (2018).
17. Kumar, A. et al. Toughness dependence of nano-bainite on phase fraction and morphology. *Mater. Sci. Eng. A* **729**, 439-443 (2018).

18. Callister Jr, W. D. et al. *Materials science and engineering an introduction.* (John Wiley & Sons, 2007).
19. Ping, D. H. et al. Metastable ω′-Fe3C carbide formed during ω-Fe3C particle coarsening in binary Fe-C alloys. *J. Appl. Phys.* **125**, 175112 (2019).
20. Ping, D.H. et al. Formation of θ-Fe3C Cementite via θ′-Fe3C (ω-Fe3C) in Fe–C Alloys. *Cryst. Growth Des.* **21**, 1683-1688 (2021).
21. Shang, Z. et al. Tailoring the strength and ductility of T91 steel by partial tempering treatment. *Acta Mater.* **169**, 209-224 (2019).
22. Ping, D. H. et al. Lath formation mechanisms and twinning as lath martensite substructures in an ultra low-carbon iron alloy. *Sci. Rep.* **8**, 14264 (2018).
23. Shah, M. et al. Wear Mechanism of High Chromium White Cast Iron and Its Microstructural Evolutions During the Comminution Process. *Tribol. Lett.* **68**, 77 (2020).
24. Dannoshita, H. et al. Evolution of dislocation structure determined by neutron diffraction line profile analysis during tensile deformation in quenched and tempered martensitic steels. *Mater. Sci. Eng. A* **854**, 143795 (2022).
25. Saastamoinen, A. et al. Direct-quenched and tempered low-C high-strength structural steel: The role of chemical composition on microstructure and mechanical properties. *Mater. Sci. Eng. A* **760**, 346-358 (2019).
26. Bhadeshia, H. et al. *Steels: microstructure and properties*. (Butterworth-Heinemann, 2017).
27. Caballero, F. G. et al.Very strong bainite. *Curr. Opin. Solid State Mater. Sci.* **8**, 251-257 (2004).
28. Kang, J. et al. Effect of tempering on the microstructure and mechanical properties of a medium carbon bainitic steel. *Mater. Sci. Eng. A* **686**, 150-159 (2017).